Fast Electron Thermometry for Ultrasensitive Calorimetric Detection

S. Gasparinetti,[1,*] K. L. Viisanen,[1,†] O.-P. Saira,[1] T. Faivre,[1] M. Arzeo,[2] M. Meschke,[1] and J. P. Pekola[1]

[1]*Department of Applied Physics, Low Temperature Laboratory, Aalto University School of Science, P.O. Box 15100, FI-00076 Aalto, Finland*

[2]*Department of Microtechnology and Nanoscience, Quantum Device Physics Laboratory, Chalmers University of Technology, SE-41296 Göteborg, Sweden*

(Received 29 May 2014; revised manuscript received 4 November 2014; published 22 January 2015)

We demonstrate radio-frequency thermometry on a micrometer-sized metallic island below 100 mK. Our device is based on a normal-metal–insulator–superconductor tunnel junction coupled to a resonator with transmission readout. In the first generation of the device, we achieve 90 $\mu\mathrm{K}/\sqrt{\mathrm{Hz}}$ noise-equivalent temperature with 10 MHz bandwidth. We measure the thermal relaxation time of the electron gas in the island, which we find to be of the order of 100 μs. Such a calorimetric detector, upon optimization, can be seamlessly integrated into superconducting circuits, with immediate applications in quantum-thermodynamics experiments down to single quanta of energy.

DOI: 10.1103/PhysRevApplied.3.014007

I. INTRODUCTION

Thermometry is a key in studies of thermodynamics. When investigating large systems, it is often sufficient to monitor time-averaged temperatures, as the relative fluctuations are small. Then the bandwidth of the thermometer may not be an important figure of merit. In small systems, on the contrary, temporal statistical variations become increasingly important and it would be of great benefit to determine the effective temperature over time scales shorter than the relevant thermal relaxation time of the measured system. Despite the apparent lack of fast thermometers in mesoscopic structures, interesting experiments in thermal physics have been performed and are under way, including measurements of the quantum of heat conductance [1–3], of Landauer's principle of minimum energy cost of erasure of a logic bit [4], and of information-to-energy conversion in Maxwell's demons [5,6]. Fast thermometry and calorimetry would tremendously expand the variety of phenomena to be explored, providing direct access to the temporal evolution of effective temperatures under nonequilibrium conditions, the energy-relaxation rates, and the fundamental fluctuations of the effective temperature in small systems. The observation of single quanta of microwave photons would eventually provide a way to investigate heat transport and its statistics in depth [7–9], for example, in superconducting quantum circuits.

Here we demonstrate a significant step towards single-microwave-photon calorimetry beyond the seminal experiments in Refs. [10–13], down to electronic temperatures below 100 mK. Our rf-transmission readout of a normal-metal–insulator–superconductor (*N*-*I*-*S*) tunnel junction provides 90-$\mu\mathrm{K}\sqrt{\mathrm{Hz}}$ thermometry with a bandwidth of 10 MHz. Based on real-time characterization of the thermal response of the island, we conclude that the measured 100-μs relaxation time would allow us to detect a 10 mK temperature spike in a single-shot measurement. Our single-shot resolution has to be enhanced by 1 order of magnitude in order to finally detect a single 1-K (20 GHz) photon impinging on an optimized absorber.

II. CHARACTERIZATION

Our technique relies on the temperature-dependent conductance of the *N*-*I*-*S* junction [14–16]. In the standard dc configuration, the high impedance of the junction, together with stray capacitance from the measurement cables, limits its bandwidth to the kilohertz range. In order to enable a fast readout, we embed the *N*-*I*-*S* junction in an *LC* resonant circuit [11]. Similar techniques are routinely used for the fast readout of high-impedance nanodevices, including single-electron transistors [17] and quantum point contacts [18,19].

Our sample consists of a 25-nm-thick, 100-nm-wide, and 20-μm-long Cu island connected to Al leads via two clean normal-metal–superconductor (*N*-*S*) contacts and a *N*-*I*-*S* junction with normal-state resistance $R_T = 22\ \mathrm{k\Omega}$. A schematic of our measurement setup is shown in Fig. 1(a) and a close-up, false-color micrograph of the device is shown in Fig. 1(b). The device is fabricated on top of an oxidized silicon substrate by standard electron-beam lithography, three-angle metal evaporation with *in situ* Al oxidation, and liftoff. The *N*-*I*-*S* probe is embedded in an *LC* resonator formed by a $L = 80$ nH surface-mount inductor, which together with the stray capacitance $C = 0.5$ pF and coupling capacitors $C_{C1} = 0.1$ pF, $C_{C2} = 0.2$ pF gives a resonant frequency $f_0 = 625$ MHz. A bias tee allows a dc voltage bias V_b to be applied to the *N*-*I*-*S* junction without

*simone.gasparinetti@aalto.fi
†klaara.viisanen@aalto.fi

interfering with the resonator readout. Of the two *N*-*S* contacts, one is grounded at the sample stage, while the other is used to feed a heating current to the island. The total resistance between the normal electrode of the *N*-*I*-*S* junction and the ground, including the resistance of the *N*-*S* contact, was measured to be 360 Ω.

We probe the resonator, coupled to input and output ports via the capacitors C_{C1} and C_{C2}, by measuring the transmittance $|S_{21}|^2 = P_{\rm det}/P_{\rm gen}$; see Fig. 1(a). For the time-resolved measurements described in the following, the signal is demodulated at the carrier frequency and recorded with a fast digitizer. The rf input line is attenuated by 80 dB below 2 K before reaching the sample stage. Two

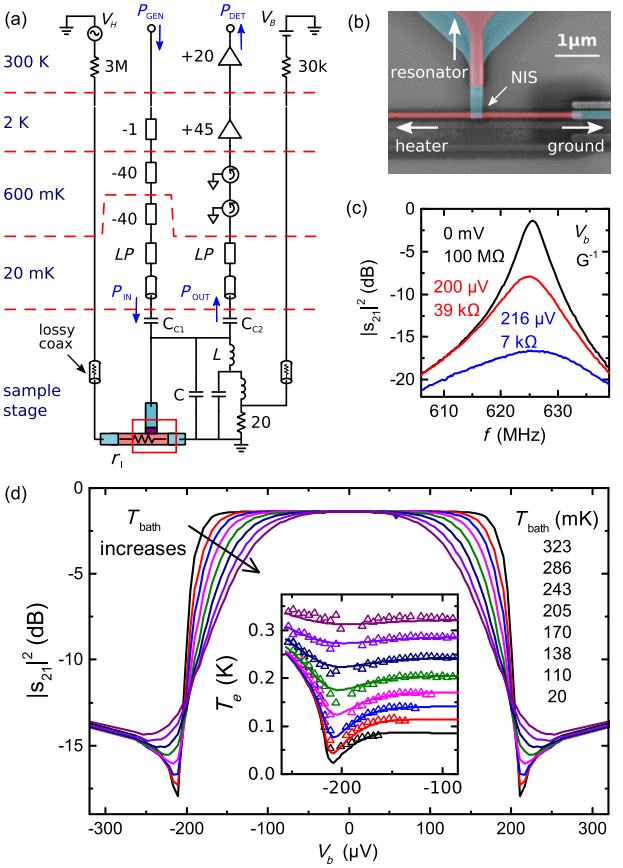

FIG. 1. The rf *N*-*I*-*S* thermometer. (a) Schematic of the measurement circuit. (b) False-color micrograph of a representative device (red, Cu; blue, Al), closing up on the *N*-*I*-*S* junction used as a thermometer. (c) Small-signal transmittance $|s_{21}|^2$ versus frequency for three selected values of the voltage bias V_b; the corresponding differential resistance G^{-1} of the *N*-*I*-*S* junction varies between 7 kΩ and 100 MΩ. (d) Transmittance-voltage characteristics: $|s_{21}|^2$ versus V_b for a set of bath temperatures $T_{\rm bath}$ in the range of 20 to 323 mK. For each temperature, the transmittance at zero bias is taken as the 0-dB reference. Inset: Electronic temperature T_e versus V_b for different values of $T_{\rm bath}$. The experimental points (triangles) are obtained from the data of the main panel using Eqs. (1) and (2). The predictions of a thermal model taking into account electron-phonon and tunneling heat conductance [20] are shown for comparison (solid lines).

circulators in series ensure at least 45-dB isolation between the resonator output and a low-noise high-electron-mobility-transistor (HEMT) amplifier mounted on the 2-K plate. The bias and heating lines are filtered by a 2-m-long lossy coaxial line (Thermocoax). Sample and resonator are enclosed in a rf-tight, indium-sealed [21] copper box mounted at the base plate of a dilution refrigerator cooled down to 20 mK. The base-plate temperature $T_{\rm bath}$ is measured by a calibrated ruthenium oxide thermometer.

At low input power, the resonator probes the differential conductance $G = \partial I/\partial V_b$ of the junction at the bias point V_b. Figure 1(c) shows how the resonance peak responds to changes in V_b. The transmittance of the resonator at resonance is given by

$$|s_{21}| = 2\kappa \frac{G_0}{G + G_0}, \tag{1}$$

with $\kappa = C_{C1}C_{C2}/(C_{C1}^2 + C_{C2}^2)$ and $G_0 = 4\pi^2(C_{C1}^2 + C_{C2}^2)Z_0 f_0^2$ (here $Z_0 = 50$ Ω is the transmission-line impedance and f_0 is the resonance frequency). By measuring $|s_{21}|^2$ at $V_b = 0$ and $V_b \gg \Delta/e$, where $G \ll G_0$ and $G \approx R_T^{-1}$, respectively, we estimate $G_0 \approx 22$ μS. For each curve in Fig. 1(c), we note the corresponding differential resistance G^{-1}, emphasizing the high sensitivity of the readout at impedances of the order of $1/G_0 \approx 50$ kΩ. At that impedance, the bandwidth, defined as the FWHM of the resonance curve, is 10 MHz and the loaded Q factor is 62.5. In the following we will probe the resonator at resonance.

With the calibrated resonator parameters κ and G_0, a measurement of the transmitted power provides the same information as the conventional current-voltage characteristics of a *N*-*I*-*S* junction. In particular, such a measurement makes it possible to infer the electronic temperature T_e in the Cu island. To extract T_e from $|s_{21}|^2$, we first convert $|s_{21}|^2$ into G using Eq. (1) and then compare the result to the expression for the conductance of the *N*-*I*-*S* junction,

$$G = \frac{1}{R_T k_B T_e} \int dE N_S(E) f(E - eV_b)[1 - f(E - eV_b)], \tag{2}$$

where k_B is the Boltzmann constant, e the electron charge, $N_S(E) = |{\rm Re}(E/\sqrt{E^2 - \Delta^2})|$ the normalized Bardeen-Cooper-Schrieffer superconducting density of states, $f(E) = [1 + \exp(E/k_B T_e)]^{-1}$ the Fermi function, and Δ is the superconducting gap. Notice that the temperature of the superconducting electrode does not appear in Eq. (2); this is a well-known property of the *N*-*I*-*S* thermometer [22]. Moreover, at low bias voltages, the backflow of heat from the superconductor is not significant at these temperatures [23].

In Fig. 1(d), we plot $|s_{21}|^2$ as a function of V_b for a set of bath temperatures $T_{\rm bath}$ in the range of 20 to 325 mK. The

corresponding T_e versus V_b, as extracted from the traces in the main panel, is plotted in the Fig. 1(d) inset (triangles). We have excluded points around $V_b = \Delta/e$, where the first-order temperature sensitivity vanishes. At base temperature $T_{\rm bath} = 20$ mK, we find that $T_e \approx 85$ mK. This saturated T_e corresponds to a spurious injected power $\dot{Q}_0 \approx 400$ aW [20], which we ascribe to imperfect shielding of blackbody radiation as well as low-frequency noise in the dc lines and in the ground potential. The dependence of T_e on V_b, most pronounced for the lowest-temperature traces, is due to heat transport across the N-I-S junction. In particular, cooling is expected to take place when $V_b \approx \Delta/e$ [24], and heating when $V_b \geq \Delta/e$. Conversely, at high temperatures, T_e closely follows $T_{\rm bath}$, as the electron-phonon heat conductance provides a strong thermal anchoring to the electrons in the Cu island. The agreement between T_e and $T_{\rm bath}$ establishes the validity of the rf N-I-S electron thermometry. Furthermore, our data are quantitatively accounted for by a simple thermal model which takes the most relevant heat flows into account [20]. The calculated T_e (solid lines) agrees well with the measured ones, except in the vicinity of the optimal cooling point, where only a modest cooling is observed if compared to the theoretical prediction. This behavior can be ascribed to local overheating of the superconductor [25], not included in the model.

III. TIME-RESOLVED MEASUREMENTS

We demonstrate the real-time capability of our thermometer by measuring the thermal relaxation of the electron gas in the Cu island in response to a Joule heating pulse. The heating pulse is generated by feeding an amplitude-modulated sinusoid of frequency $f_H = 1$ MHz to a large bias resistor, resulting in an ac heating current of peak-to-peak amplitude $I_H^{\rm pp}$. Because f_H is much faster than the measured thermal relaxation rates (see the following), the island reacts to a time-averaged heating power $\dot{Q}_H \propto (I_H^{\rm pp})^2$ when the heating is on. The time-domain response of the thermometer to the heating pulse is shown in Fig. 2(b) at base temperature, for a fixed V_b and different values of $I_H^{\rm pp}$. The left axis indicates the instantaneous power recorded by the digitizer. This power is converted into temperature using a similar procedure as in the Fig. 1(d) inset, and the corresponding scale is noted on the right axis. The temperature reached by the island at the end of the heating pulse is plotted in the Fig. 2(b) inset as a function of $I_H^{\rm pp}$ (triangles), in good agreement with the prediction of the thermal model (solid line). From Fig. 2, we see that the thermal response of the island is not instantaneous; instead, a finite-time relaxation is observed after the rising and falling edge of the pulse.

With constant heat input and when T_e is not far from its steady-state value $T_{e,0}$, the heat equation governing

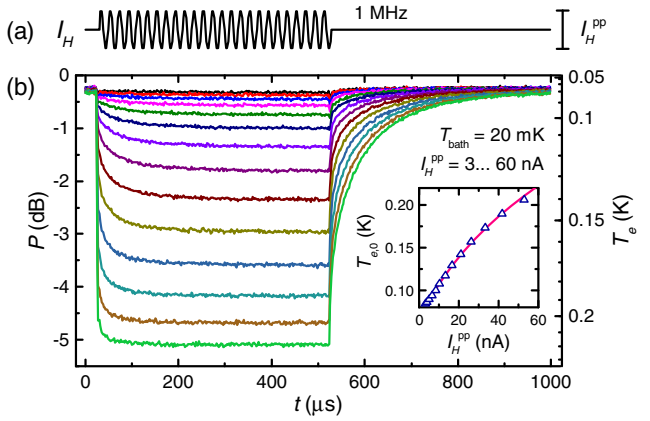

FIG. 2. Time-resolved thermometry. (a) Amplitude-modulated sinusoid used to drive the heating pulse (the frequency is not to scale) and (b) real-time response of the thermometer, obtained by recording the transmitted power P versus time for different values of the heating-pulse amplitude $I_H^{\rm pp}$. The conversion from P into absolute electronic temperature T_e is displayed on the right axis. Inset: T_e at the end of the heating pulse ($t = 520$ μs) versus $I_H^{\rm pp}$ (triangles). The prediction of the thermal model [20] is shown for comparison (solid line). All the traces are taken at base temperature by averaging over 10^4 heating cycles and the voltage bias is $V_b = 0.17$ mV.

the temperature deviation $\delta T = T_e - T_{e,0}$ can be written as

$$\mathcal{C}\frac{d\delta T}{dt} = -G_{\rm th}\delta T, \tag{3}$$

where $\mathcal{C}$ is the electronic heat capacity of the island and $G_{\rm th}$ the thermal conductance to its heat bath. Equation (3) tells us that T_e relaxes to $T_{e,0}$ exponentially with the relaxation time $\tau = \mathcal{C}/G_{\rm th}$, where $\mathcal{C}$ and $G_{\rm th}$ are to be evaluated at $T_e = T_{e,0}$. Even after a large change in the heating power [beyond the linear-response regime described by Eq. (3)], the final approach to the new $T_{e,0}$ obeys this exponential law. The value of $\mathcal{C}$ is ideally given by the standard expression for a Fermi electron gas, $\mathcal{C} = \gamma\mathcal{V}T_{e,0}$, where $\gamma = 71$ J K^{-2} m^{-3} [26] and $\mathcal{V}$ is the volume of the island (in our case, $\mathcal{V} = 0.05$ μm^3). On the other hand, $G_{\rm th}$ is determined by the sum of all relevant parallel heat conductances. In the present case, we expect the electron-phonon heat conductance $G_{\rm th,NIS}$ and the tunneling heat conductance through the biased N-I-S junction $G_{\rm th,NIS}$ to be the dominant contributions. Heat transport through the clean N-S contacts can be neglected [27] and photonic heat conductance is also negligible for our sample at these temperatures, due to the mismatch of the relevant impedances [28]. Measurements of the heat conductance out of a metallic island were recently reported in Ref. [29]. The standard expression for $G_{\rm th,}e\text{-ph}$ is quoted as $G_{\rm th,}e\text{-ph} = 5\Sigma\mathcal{V}T_e^4$ [30,31]; however, other power laws in T_e have also been reported for experiments on Cu islands

[32,33]. The tunneling heat conductance is given by $G_{\mathrm{th,NIS}} = -\frac{1}{e^2 R_T k_B T^2}\int_{-\infty}^{\infty} dE N_S(E)(E-\mathrm{eV})^2 f(E-\mathrm{eV})\times[1-f(E-\mathrm{eV})]$. For our relatively large island and according to these expressions, we expect $G_{\mathrm{th},e\text{-ph}} \gg G_{\mathrm{th,NIS}}$ when the junction is biased far from the gap and $G_{\mathrm{th},e\text{-ph}} \approx G_{\mathrm{th,NIS}}$ when V_b approaches Δ/e. However, as indicated by the data in the Fig. 1(d) inset, the cooling performance of the *N-I-S* junction is degraded when $V_b \approx \Delta/e$, possibly implying a weaker $G_{\mathrm{th,NIS}}$ than predicted by the model. Finally, it should be mentioned that the electron-phonon relaxation times reported in Refs. [12,32] were longer than those expected based on the expressions above. In addition to a nonideal $G_{\mathrm{th},e\text{-ph}}$, this may suggest a heat capacity 1 order of magnitude larger than described by the Fermi gas model, possibly due to magnetic impurities in the metal film [34,35]. Furthermore, overheating of the local phonon bath, considered in a recent experiment [36], may also lead to longer relaxation times, due to the additional series thermal resistance between the local phonon bath and the thermalized substrate phonons.

We estimate the thermal relaxation times τ_{rise} and τ_{fall} by fitting an exponential function to the tails of the relaxation traces observed in Fig. 2 after the rising (τ_{rise}) and falling edge (τ_{fall}) of the heating pulse [37]. More details on the fitting procedure are given in the Supplemental Material [20]. As we increase the pulse amplitude I_H^{pp}, we observe a decrease in τ_{rise}, which is consistent with thermal relaxation to a higher temperature. On the other hand, τ_{fall} does not depend on I_H^{pp}, as expected due to the fact that the relaxation temperature stays the same. We have repeated the measurements of Fig. 2 while varying the bias voltage V_b and the bath temperature T_{bath}. The corresponding relaxation times τ are shown in Fig. 3. In panel 3(a), we show the dependence on V_b for two different values of T_{bath}. The measured τ at base temperature is of the order of 100 μs and it increases by some 20% as V_b approaches Δ/e. This increase may well be due to a decrease in $G_{\mathrm{th},e\text{-ph}}$ upon cooling of the island [compare the Fig. 1(d) inset]. In panel 3(b), we show the temperature dependence of τ, obtained in two independent ways. We first measured τ_{fall} while varying T_{bath} (circles) and then τ_{rise} while varying I_H^{pp} (triangles). τ_{fall} is plotted against T_{bath} and τ_{rise} is plotted against $T_{e,0}$ at the end of the pulse, estimated as in Fig. 2(b). The agreement between the two series is remarkable. The saturation of τ at low T_{bath} is also consistent with the saturated T_e observed in the Fig. 1(d) inset. From the measured τ, we estimate a heat capacity $\mathcal{C} = 2\times 10^5 k_B = 3$ aJ/K, 1 order of magnitude larger than the expected value for a Cu island of the size and temperature in this experiment. At higher temperatures, τ is predicted to scale as $T_{e,0}^{-3}$ provided $G_{\mathrm{th}} \approx G_{\mathrm{th},e\text{-ph}}$ and both $\mathcal{C}$ and $G_{\mathrm{th},e\text{-ph}}$ follow the theory predictions. The data presented here are not conclusive in this respect, due to the saturation of $T_{e,0}$ at low T_{bath} and to the narrow temperature range considered. This range is not limited by the bandwidth of our thermometer, but rather by a transient that we observe after terminating the heat pulse, possibly due to the heavy low-pass filtering applied to the heating line. For this reason, we refrain from presenting data points with $\tau \lesssim 20$ μs and leave the study of relaxation times down to 1 μs and below to future investigation.

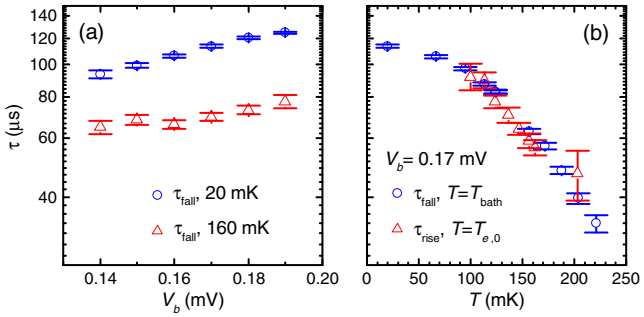

FIG. 3. Thermal relaxation times. (a) Thermal relaxation time τ versus voltage bias V_b for two different values of the bath temperature T_{bath}. (b) Temperature dependence of τ, as estimated from relaxation after the falling edge (circles; the x axis is T_{bath}) as well as the rising edge of the pulse (triangles; the x axis is the temperature $T_{e,0}$ at the end of the pulse). The error bars are obtained from the fits (see the Supplemental Material [20]).

IV. NOISE AND RESPONSIVITY

We have performed an extensive characterization of the responsivity and noise of the thermometer readout. Our first set of experiments, presented above, were performed at low input powers corresponding to a voltage modulation amplitude across the *N-I-S* junction of the order of 1 μV. In this case, the readout probes the local differential conductance of the junction. Accordingly, the theoretical responsivity $\mathcal{R} = \partial P_{\mathrm{det}}/\partial T_e$ of the thermometer is $\mathcal{R} \propto P_{\mathrm{gen}}(\partial|s_{21}|^2/\partial G)(\partial G/\partial T_e)$. We evaluate the noise-equivalent temperature (NET) as $(\delta P_{\mathrm{det}}/\delta T)^{-1}(\sqrt{S_{P_{\mathrm{det}}P_{\mathrm{det}}}})$, where $S_{P_{\mathrm{det}}P_{\mathrm{det}}}$ is the measured noise spectral density of the detected power P_{det}. At an electron temperature of 80 mK and at the optimal bias point of 0.17 mV, we obtain our best NET of 90 $\mu\mathrm{K}/\sqrt{\mathrm{Hz}}$. We always find an essentially white-noise spectrum, with a corner frequency for $1/f$ noise of the order of a few hertz.

The thermometer readout was amplifier limited. We characterize the noise of the rf readout chain by the system noise temperature T_{sys} referred to the output port of the sample box. In this case (see the Supplemental Material for details [20]), one has $S_{P_{\mathrm{det}}P_{\mathrm{det}}} \approx 4\mathcal{G}k_B T_{\mathrm{sys}} P_{\mathrm{det}}$, where $\mathcal{G} = P_{\mathrm{det}}/P_{\mathrm{out}}$ is the total gain of the amplification chain. Using power-dependent features of the *N-I-S*-junction-loaded resonator as markers, we estimate $\mathcal{G} = 55 \pm 1$ dB and $T_{\mathrm{sys}} = 62 \pm 15$ K. The discrepancy between T_{sys} and the nominal noise temperature of the HEMT amplifier,

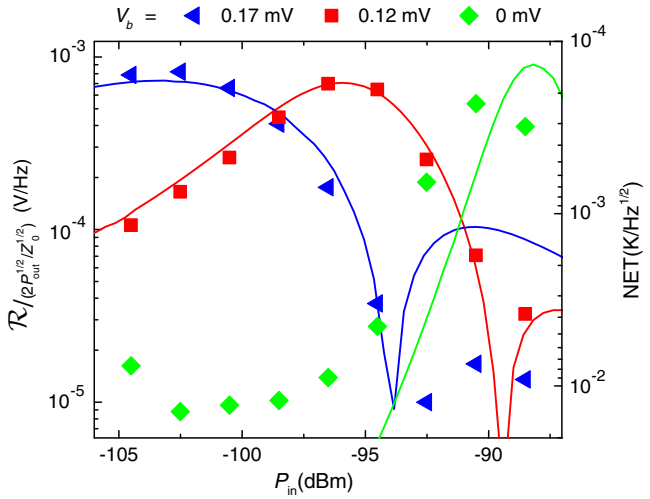

FIG. 4. Power optimization. Normalized responsivity $\mathcal{R}$ (left axis) and corresponding noise-equivalent temperature (right axis) versus $P_{\rm in}$ for three selected bias voltages (symbols), measured at 150 mK. Numerical simulations are shown for comparison (solid lines; see the Supplemental Material [20] for details).

13.3 K at 640 MHz, suggests an insertion loss of the order of 7 dB between the resonator and the amplifier.

Assuming the heat conductance $G_{\rm th}$ to be dominated by electron-phonon interaction [as indicated by the steady-state measurements of Fig. 1(d)], the noise-equivalent power (NEP) is given by $\mathrm{NEP} = \mathrm{NET} \times G_{\rm th} = 2.5e{-}18\ \mathrm{W}/\sqrt{\mathrm{Hz}}$. This figure is 1 order of magnitude above the thermal fluctuation noise limit $\mathrm{NEP}_{\rm th} = \sqrt{4k_B T_e^2 G_{\rm th}} = 1 \times 10^{-19}\ \mathrm{W}/\sqrt{\mathrm{Hz}}$.

One may ask whether the NET figure given above can be significantly improved by operating the rf–*N*-*I*-*S* thermometer at higher input powers, i.e., beyond the linear regime. In Fig. 4, we compare the responsivity and NET of our thermometer at different bias voltages and as a function of the power fed to the input line. The data (symbols) were taken in a separate cooldown using an equivalent setup and a sample with $R_T = 28\ \mathrm{k\Omega}$. The optimal power increases as the bias point is shifted towards zero bias. Importantly, a sensitivity close to the global optimum ($144\ \mu\mathrm{K}/\sqrt{\mathrm{Hz}}$ for this sample at $T_{\rm bath} = 150$ mK) is reached over a broad range of bias voltages by a suitable choice of probing power. This feature can be understood by considering the combined contribution of the dc bias and the rf drive to the instantaneous voltage across the junction, and the fact that the responsivity of the *N*-*I*-*S* thermometer is concentrated in a narrow voltage range slightly below the superconducting gap edge. Indeed, full numerical simulations (solid lines) confirm this behavior.

V. OUTLOOK

In summary, we have demonstrated an electronic thermometer with promise for ultralow-energy calorimetry, operating below 100 mK, with $90\ \mu\mathrm{K}/\sqrt{\mathrm{Hz}}$ noise-equivalent temperature and 10 MHz bandwidth. We have measured thermal relaxation times up to 100 μs, in line with 1.6–20 μs measured by other methods at higher temperatures [12,32]. These figures already enable single-shot detection of an energy-absorption event producing a 10 mK temperature spike. Such a spike could be generated, for instance, by a single terahertz photon impinging of an absorber of reduced volume, as well as by a multiphoton wave packet in the *C* and *X* band used for superconducting-quantum-bit readout [38–40]. In absolute terms, the NEP performance of our device still lags behind that of state-of-the-art transition-edge sensors [41,42] and semiconductor bolometers [43,44], which routinely achieve NEPs of the order of $10^{-20}\ \mathrm{W}/\sqrt{\mathrm{Hz}}$. However, most of these devices are intended for detection of terahertz radiation, while our primary focus is on microwave photons. In the microwave domain, our approach presents some advantages; in particular, our sensor can be straightforwardly integrated in superconducting coplanar waveguides, acting as a lumped-element resistor whose impedance can be made to be of the order of 50 Ω.

Our current device and setup leave room for improvement. Calculations indicate that the sensitivity of a fully optimized *N*-*I*-*S* thermometer can reach $\mathrm{NET}_{\rm opt} = \sqrt{2.72 e^2 T_{\rm sys} R_T / k_B}$. Using the parameters for our primary sample ($R_T = 22\ \mathrm{k\Omega}$) and present setup ($T_{\rm sys} = 62$ K), this formula yields $\mathrm{NET}_{\rm opt} = 83\ \mu\mathrm{K}/\sqrt{\mathrm{Hz}}$, to be compared with our experimental value of $90\ \mu\mathrm{K}/\sqrt{\mathrm{Hz}}$. We conclude that the impedance matching between the *N*-*I*-*S* junction and the transmission line realized by the resonator was close to optimal. Instead, the system noise temperature could be lowered by more than an order of magnitude by reducing losses between the sample box and the amplifier and by employing an amplifier with a lower noise temperature as the first stage; a Josephson parametric amplifier [45] is one such choice. The energy resolution of our detector can be estimated as $\delta E = \mathcal{C}\delta T = \mathrm{NET} \times \mathcal{C}\tau^{-1/2}$. For the present case, this gives $\delta E = 2.3 \times 10^{-20}$ J, corresponding to a photon of frequency $\delta E/h = 34$ THz. The measured sample was not optimized for obtaining a small energy resolution; instead, we aimed at a strong coupling between the island and the phonon bath. In order to boost energy resolution, the size of the island can be made significantly smaller, which is the next step toward improving this device. When the noise is limited by thermal fluctuations, we can write $\delta E = \sqrt{4k_B \mathcal{V}\gamma^2/(5\Sigma\tau)}$. For a sample with 50 times smaller island limited by thermal fluctuations, the energy resolution at 80 mK, assuming 100-μs relaxation time, is $\delta E/h = 30$ GHz. Since τ increases strongly with decreasing temperature, lowering the island temperature is another key point. Optimized as indicated, our detector will facilitate a series of experiments

of fundamental relevance in classical and quantum thermodynamics, as well as calorimetric measurements of dissipation down to single microwave photons in superconducting quantum circuits.

ACKNOWLEDGMENTS

We would like to thank A. Adamyan, S. Kubatkin, J. Govenius, R. Lake and J. Peltonen for useful discussions and S. Kafanov for technical assistance at an early stage of the project. This work has been supported in part by the Academy of Finland (Projects No. 139172 and No. 250280), and the European Union Seventh Framework Programme INFERNOS (FP7/2007-2013) under Grant Agreement No. 308850. S. G. acknowledges financial support from the Finnish National Graduate School in Nanoscience (NGS-NANO) and from the Aalto Doctoral Programme in Science. We acknowledge the provision of facilities and technical support by Aalto University at Micronova Nanofabrication Centre.

[1] K. Schwab, E. A. Henriksen, J. M. Worlock, and M. L. Roukes, Measurement of the quantum of thermal conductance, Nature (London) **404**, 974 (2000).

[2] M. Meschke, W. Guichard, and J. P. Pekola, Single-mode heat conduction by photons, Nature (London) **444**, 187 (2006).

[3] S. Jezouin, F. D. Parmentier, A. Anthore, U. Gennser, A. Cavanna, Y. Jin, and F. Pierre, Quantum limit of heat flow across a single electronic channel, Science **342**, 601 (2013).

[4] A. Bérut, A. Arakelyan, A. Petrosyan, S. Ciliberto, R. Dillenschneider, and E. Lutz, Experimental verification of Landauer's principle linking information and thermodynamics, Nature (London) **483**, 187 (2012).

[5] S. Toyabe, T. Sagawa, M. Ueda, E. Muneyuki, and M. Sano, Experimental demonstration of information-to-energy conversion and validation of the generalized Jarzynski equality, Nat. Phys. **6**, 988 (2010).

[6] J. V. Koski, V. F. Maisi, J. P. Pekola, and D. V. Averin, Experimental realization of a Szilard engine with a single electron, Proc. Natl. Acad. Sci. U.S.A. **111**, 13786 (2014).

[7] J. P. Pekola, P. Solinas, A. Shnirman, and D. V. Averin, Calorimetric measurement of work in a quantum system, New J. Phys. **15**, 115006 (2013).

[8] S. Gasparinetti, P. Solinas, A. Braggio, and M. Sassetti, Heat-exchange statistics in driven open quantum systems, New J. Phys. **16**, 115001 (2014).

[9] M. Silaev, T. T. Heikkilä, and P. Virtanen, Lindblad-equation approach for the full counting statistics of work and heat in driven quantum systems, Phys. Rev. E **90**, 022103 (2014).

[10] M. Nahum and J. M. Martinis, Hot-electron microcalorimeters as high-resolution x-ray detectors, Appl. Phys. Lett. **66**, 3203 (1995).

[11] D. R. Schmidt, C. S. Yung, and A. N. Cleland, Nanoscale radio-frequency thermometry, Appl. Phys. Lett. **83**, 1002 (2003).

[12] D. R. Schmidt, C. S. Yung, and A. N. Cleland, Temporal measurement of hot-electron relaxation in a phonon-cooled metal island, Phys. Rev. B **69**, 140301(R) (2004).

[13] D. R. Schmidt, K. W. Lehnert, A. M. Clark, W. D. Duncan, K. D. Irwin, N. Miller, and J. N. Ullom, A superconductor-insulator-normal metal bolometer with microwave readout suitable for large-format arrays, Appl. Phys. Lett. **86**, 053505 (2005).

[14] J. M. Rowell and D. C. Tsui, Hot electron temperature in InAs measured by tunneling, Phys. Rev. B **14**, 2456 (1976).

[15] M. Nahum and J. M. Martinis, Ultrasensitive-hot-electron microbolometer, Appl. Phys. Lett. **63**, 3075 (1993).

[16] F. Giazotto, T. T. Heikkilä, A. Luukanen, A. M. Savin, and J. P. Pekola, Opportunities for mesoscopics in thermometry and refrigeration: Physics and applications, Rev. Mod. Phys. **78**, 217 (2006).

[17] R. J. Schoelkopf, P. Wahlgren, A. A. Kozhevnikov, and D. E. Prober, The radio-frequency single-electron transistor (RF-SET): A fast and ultrasensitive electrometer, Science **280**, 1238 (1998).

[18] H. Qin and D. A. Williams, Radio-frequency point-contact electrometer, Appl. Phys. Lett. **88**, 203506 (2006).

[19] D. J. Reilly, C. M. Marcus, M. P. Hanson, and A. C. Gossard, Fast single-charge sensing with a rf quantum point contact, Appl. Phys. Lett. **91**, 162101 (2007).

[20] See Supplemental Material at http://link.aps.org/supplemental/10.1103/PhysRevApplied.3.014007 for details on the thermal model mentioned in the text, the extraction of thermal relaxation times, the responsivity at high powers, and noise measurements.

[21] O.-P. Saira, A. Kemppinen, V. F. Maisi, and J. P. Pekola, Vanishing quasiparticle density in a hybrid Al/Cu/Al single-electron transistor, Phys. Rev. B **85**, 012504 (2012).

[22] H. Pothier, S. Guéron, N. O. Birge, D. Esteve, and M. H. Devoret, Energy Distribution Function of Quasiparticles in Mesoscopic Wires, Phys. Rev. Lett. **79**, 3490 (1997).

[23] J. Muhonen, M. Meschke, and J. P. Pekola, Micrometre-scale refrigerators, Rep. Prog. Phys. **75**, 046501 (2012).

[24] M. Nahum, T. M. Eiles, and J. M. Martinis, Electronic microrefrigerator based on a normal-insulator-superconductor tunnel junction, Appl. Phys. Lett. **65**, 3123 (1994).

[25] S. Rajauria, H. Courtois, and B. Pannetier, Quasiparticle-diffusion-based heating in superconductor tunneling microcoolers, Phys. Rev. B **80**, 214521 (2009).

[26] B. W. Roberts, *Properties of Selected Superconductive Materials*, NBS Technical Note 983, (U.S. Government Printing Office, Washington, 1978).

[27] J. T. Peltonen, P. Virtanen, M. Meschke, J. V. Koski, T. T. Heikkilä, and J. P. Pekola, Thermal Conductance by the Inverse Proximity Effect in a Superconductor, Phys. Rev. Lett. **105**, 097004 (2010).

[28] A. V. Timofeev, M. Helle, M. Meschke, M. Möttönen, and J. P. Pekola, Electronic Refrigeration at the Quantum Limit, Phys. Rev. Lett. **102**, 200801 (2009).

[29] J. Govenius, R. E. Lake, K. Y. Tan, V. Pietilä, J. K. Julin, I. J. Maasilta, P. Virtanen, and M. Möttönen, Microwave nanobolometer based on proximity Josephson junctions, Phys. Rev. B **90**, 064505 (2014).

[30] F. C. Wellstood, C. Urbina, and J. Clarke, Hot-electron effects in metals, Phys. Rev. B **49**, 5942 (1994).

[31] M. L. Roukes, M. R. Freeman, R. S. Germain, R. C. Richardson, and M. B. Ketchen, Hot Electrons and Energy Transport in Metals at Millikelvin Temperatures, Phys. Rev. Lett. **55**, 422 (1985).

[32] L. J. Taskinen, J. M. Kivioja, J. T. Karvonen, and I. J. Maasilta, Direct measurement of the electron-phonon relaxation rate in thin copper films, Phys. Status Solidi C **1**, 2856 (2004).

[33] J. T. Karvonen, L. J. Taskinen, and I. J. Maasilta, Observation of disorder-induced weakening of electron-phonon interaction in thin noble-metal films, Phys. Rev. B **72**, 012302 (2005).

[34] F. Pobell, *Matter and Methods at Low Temperatures*, 3rd ed. (Springer, New York, 2007).

[35] A. Anthore, F. Pierre, H. Pothier, and D. Esteve, Magnetic-Field-Dependent Quasiparticle Energy Relaxation in Mesoscopic Wires, Phys. Rev. Lett. **90**, 076806 (2003).

[36] L. M. A. Pascal, A. Fay, C. B. Winkelmann, and H. Courtois, Existence of an independent phonon bath in a quantum device, Phys. Rev. B **88**, 100502 (2013).

[37] A small (<2%) baseline correction is applied to correct for a slow, much weaker relaxation process of unknown origin. See the Supplemental Material [20] for details.

[38] A. Wallraff, D. I. Schuster, A. Blais, L. Frunzio, R. S. Huang, J. Majer, S. Kumar, S. M. Girvin, and R. J. Schoelkopf, Strong coupling of a single photon to a superconducting qubit using circuit quantum electrodynamics, Nature (London) **431**, 162 (2004).

[39] A. A. Houck, D. I. Schuster, J. M. Gambetta, J. A. Schreier, B. R. Johnson, J. M. Chow, L. Frunzio, J. Majer, M. H. Devoret, S. M. Girvin, and R. J. Schoelkopf, Generating single microwave photons in a circuit, Nature (London) **449**, 328 (2007).

[40] D. Bozyigit, C. Lang, L. Steffen, J. M. Fink, C. Eichler, M. Baur, R. Bianchetti, P. J. Leek, S. Filipp, M. P. da Silva, A. Blais, and A. Wallraff, Antibunching of microwave-frequency photons observed in correlation measurements using linear detectors, Nat. Phys. **7**, 154 (2011).

[41] B. S. Karasik and R. Cantor, Demonstration of high optical sensitivity in far-infrared hot-electron bolometer, Appl. Phys. Lett. **98**, 193503 (2011).

[42] B. S. Karasik, A. V. Sergeev, and D. E. Prober, Nanobolometers for THz photon detection, IEEE Trans. Terahertz Sci. Technol. **1**, 97 (2011).

[43] S. Komiyama, O. V. Astafiev, V. Antonov, T. Kutsuwa, and H. Hirai, A single-photon detector in the far-infrared range, Nature (London) **403**, 405 (2000).

[44] S. Komiyama, Single-photon detectors in the terahertz range, IEEE J. Sel. Top. Quantum Electron. **17**, 54 (2011).

[45] M. A. Castellanos-Beltran and K. W. Lehnert, Widely tunable parametric amplifier based on a superconducting quantum interference device array resonator, Appl. Phys. Lett. **91**, 083509 (2007).